Soft Matter

PAPER

Cite this: *Soft Matter*, 2019, **15**, 5128

Entry modes of ellipsoidal nanoparticles on a membrane during clathrin-mediated endocytosis

Hua Deng, Prashanta Dutta and Jin Liu *

Received 12th April 2019,
Accepted 2nd June 2019

DOI: 10.1039/c9sm00751b

rsc.li/soft-matter-journal

The membrane wrapping and internalization of nanoparticles, such as viruses and drug nanocarriers, through clathrin-mediated endocytosis (CME) are vitally important for intracellular transport. During CME, the shape of the particle plays crucial roles in the determination of particle–membrane interactions, but much of the previous work has been focused on spherical particles. In this work, we develop a stochastic model to study the CME of ellipsoidal particles. In our model, the deformation of the membrane and wrapping of the nanoparticles are driven by the accumulation of clathrin lattices, which is stimulated by the ligand–receptor interactions. Using our model, we systematically investigate the effect of particle shape (ellipsoids with different aspect ratios) on the CME. Our results show three entry modes: tip-first, tilted, and laying-down modes, used by ellipsoidal nanoparticles for internalization depending on the aspect ratio. Certain ellipsoids are able to take multiple entry modes for internalization. Interestingly, the prolate ellipsoid with an aspect ratio of 0.42 can be internalized with a significantly reduced number of ligand–receptor bonds. Particles which can be internalized with fewer bonds are excellent candidates for transcellular drug delivery. Moreover, our results demonstrate that internalization of ellipsoids with intermediate aspect ratios is easier than that of particles with low and high aspect ratios. Our model and simulations provide critical mechanistic insights into CME of ellipsoidal particles, and represent a viable platform for optimal design of nanoparticles for targeted drug delivery applications.

1 Introduction

Clathrin-mediated endocytosis (CME) is an important route for the intracellular transport of nanoparticles such as viruses and drug agents. Many physical and chemical parameters of the nanoparticle such as size, shape and surface functionality *etc.* potentially impact the membrane wrapping and particle uptake. Most current nanoparticles designed in the lab or in clinical trials have been spherical because of fabrication easiness. However, viruses and bacteria in nature are often in non-spherical shapes.[1,2] Human cells are also capable of recognizing and ingesting non-spherical particles.[3] The recent advancement of nanofabrication techniques makes the manufacturing of various non-spherical particles possible for drug delivery and medical diagnosis.[4,5] Therefore studying the impact of the shape of nanoparticles on the membrane wrapping is of great significance for future biomedical applications. Recent experimental and theoretical studies on nanoparticle shapes have shown scattered results. The interactions between the non-spherical nanoparticles and the membrane during CME are still elusive.

School of Mechanical and Materials Engineering, Washington State University, Pullman, WA 99163, USA. E-mail: jin.liu2@wsu.edu

Experimental studies have uncovered the existence of different uptake behaviors between non-spherical and traditional spherical particles through endocytosis. Some of the studies proposed a higher internalization efficiency of spherical nanoparticles than the anisotropic counterparts. For example, Chithrani *et al.*[6] have found less nonspecific uptake of rod-shaped gold nanoparticles (AuNR) compared to gold nanospheres (AuNS) in HeLa cells. A follow up study demonstrated suppressed CME of transferrin-coated nanorods in comparison to spheres with STO, HeLa and SNB19 cells.[7] Ellipsoidal polymeric nanoparticles and polystyrene nanodisks are also found to be less internalized than the spherical counterparts.[8,9] In contrast, Barua *et al.* observed higher specific uptake of ligand-coated nanorods than nanospheres and nanodisks in breast cancer cell lines.[10] Huang *et al.*[11] also proposed higher and faster internalization of larger aspect ratio silica rod-shaped nanoparticles into A375 human melanoma cells. These controversial results illustrate the fact that the uptake of nanoparticles is highly shape, size and cell type dependent.

For nonspherical nanoparticles, the interplay between aspect ratio (AR), shape and size is complicated. Intermediate ARs are found to facilitate internalization while high ARs may suppress the uptake.[8,12] In contrast, it is found that there is a higher internalization rate of high AR rod-like nanohydrogels

than lower AR ones in HeLa cells.[13] Besides, it is also found that the optimal AR and shape for uptake are varying in different mammalian cells.[14] A higher uptake of nanodiscs with intermediate aspect ratio than nanorods was observed in endothelia cells, while high aspect ratio nanodiscs are preferred by epithelial and immune cells. The shape of nanoparticles also determines the optimal uptake size. For example, disk-like nanoparticles may have a larger optimal size than spherical particles.[15] Understanding the relationship between AR and nanoparticle uptake provides important insights for rational design of future drug carriers.

Continuum and coarse-grained molecular dynamics (CGMD) models have been developed to understand both the passive penetration and active endocytosis of spherical and nonspherical nanoparticles.[16–21] The studies have demonstrated the importance of shape in determining the nanoparticle uptake mechanisms.[21–25] Moreover, the rotation of anisotropic particles is found to play crucial roles during the membrane wrapping.[26–29] The internalization efficiency is compared between spherical and nonspherical nanoparticles. Some studies suggest a higher endocytosis rate of spherical particles than that of the ellipsoidal, rod-like and disk-shape counterparts.[26,30] In contrast, Vácha *et al.*[23] found that the internalization rate is higher for spherocylindrical particles than spheres. The influence of aspect ratio on endocytosis is also studied but still under debate. Recent studies illustrated faster internalization of solid oblate ellipsoid compared to prolate-shaped particles,[25] while other studies showed the opposite trend.[30,31]

In this work, we systematically investigate the CME of spherical and ellipsoidal nanoparticles through stochastic modeling and simulations. This model is based on our previously proved stochastic model for CME.[32] Different from previous theoretical models, in our current model the deformation of the membrane and the wrapping of the nanoparticles are driven by the accumulation of clathrin lattices, which is triggered by the ligand–receptor interactions. Using this model we explore the effects of nanoparticle AR and rotation on the overall process of endocytosis. Our results demonstrate three entry modes of the ellipsoidal nanoparticles with distinct patterns of bond formation. The particle entry mode is highly dependent on the particle shape. The simulations show consistent results with various experimental measurements and help to uncover the fundamental mechanisms involved in this complex process. The model and simulations presented in this paper may provide theoretical guidelines for optimal design of nanoparticles for targeted drug delivery.

2 Model and methods

2.1 Ellipsoidal nanoparticle

In a Cartesian coordinate system, the standard form for an ellipsoid with the center located at the origin can be expressed as:

$$\frac{x^2+y^2}{a^2}+\frac{z^2}{b^2}=1 \qquad (1)$$

The aspect ratio is defined by AR = a/b. Then we could define different nanoparticle shapes with various ARs (Fig. 1).

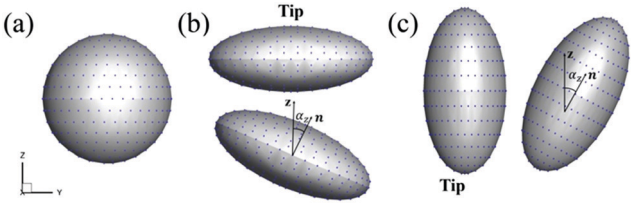

Fig. 1 Shapes of sphere, oblate-shaped and prolate-shaped ellipsoids with ligands. Blue dots are the positions for coated ligands. Unit vector $\boldsymbol{n}$ indicates the direction of the ellipsoidal nanoparticle. α_z is the angle between vector $\boldsymbol{n}$ and the z-axis. (a) Spherical nanoparticle AR = 1. (b) Oblate-shaped ellipsoid with AR = 2.5. (c) Prolate-shaped nanoparticle with AR = 0.5.

If AR $>$ 1, the ellipsoid is oblate-shaped, and if AR $<$ 1, the ellipsoid is prolate-shaped. If AR = 1 then the nanoparticle is a sphere.

The tip orientation is defined along the major and minor axes of the prolate- and oblate-shaped ellipsoids, respectively. Thus, the oblate-shaped ellipsoid has a flat tip while the prolate-shaped ellipsoid has a highly curved tip. The unit vector $\boldsymbol{n}$ defines the orientation of the nanoparticle. It rotates together with the rotation of the nanoparticle during the simulations such that we can trace the orientation of the nanoparticle. α_z defines the angle between vector $\boldsymbol{n}$ and the z-axis of the coordinate system. The nanoparticle is not allowed to rotate before having at least two ligand–receptor bonds in order to precisely control the initial attack angle of the nanoparticle to the membrane surface. After that, the nanoparticle is able to freely rotate.

2.2 Clathrin-mediated endocytosis model

In our model, the ligands are approximated as cylinders and uniformly distributed on the surface of the rigid nanoparticle (Fig. 1). The nanoparticle is able to translate and rotate. The ligands and receptors are modeled as cylinders with one end attached to the particle/membrane surface and the other free end as the binding tip. The receptors are placed normal to the local surface and can freely diffuse on the membrane. The membrane surface is modeled with the Helfrich Hamiltonian.[33,34] The total energy E of the membrane is:

$$E=\iint\left[\frac{\kappa}{2}(2H-H_0)^2+\bar{\kappa}K+\sigma\right]\mathrm{d}A \qquad (2)$$

where κ and $\bar{\kappa}$ are the bending rigidity and Gaussian rigidity of the membrane, and σ represents the membrane tension. $H=(c_1+c_2)/2$ is the mean curvature and $K=c_1c_2$ is the Gaussian curvature of the surface; c_1 and c_2 are the principal radii of curvature. H_0 is the intrinsic or spontaneous mean curvature of the membrane. Recent work has demonstrated the critical roles of intrinsic curvature in selection of particle size and shape during endocytosis.[35,36] The Gaussian term remains a constant and is hence not included in the model, because of the fixed topology of the membrane during the simulation. The parameters in eqn (2) depend on the properties of the membrane bilayer, local protein expressions and cytoskeleton networks *etc.*[37–39] In this work the membrane

properties (κ and σ) are fixed (see Table 3). In our model as illustrated in Fig. 2, the membrane surface is discretised in a triangulated system,[40,41] which consists of a number of vertices connected by links. The deformation is through the displacement of vertices and flipping of links,[42] each movement affecting the membrane energy in eqn (2).

During CME, the accumulation of clathrin-coated pits (CCPs) plays key roles in driving the deformation of the membrane. Experiments have shown that the energetically favorable shape of a CCP is a spherical-shape structure.[43,44] The indispensable role of a CCP for driving the deformation is also observed.[45] In addition, it has been shown that a CCP alone provides sufficient curvature to bend the membrane for budding. The underling mechanism of CCP transformation from a flat to a curved shape is extremely complicated involving the coordination of many factors, such as the adaptor proteins (APs), topological disclinations and clathrin network elasticity.[46–49] In our model, the effect of the CCP is simplified and modeled as an additional intrinsic curvature H_{cla} with higher bending rigidity κ_{cla}. Therefore, the total energy of the membrane with clathrin can be expressed as:

$$E = \iint \left[\frac{\kappa}{2}(2H)^2 + \sigma\right] \mathrm{d}A + \iint \left[\frac{\kappa_{\mathrm{cla}}}{2}(2H - H_{\mathrm{cla}})^2\right] \mathrm{d}A \qquad (3)$$

where κ_{cla} = 200 $k_{\mathrm{B}}T$ [50] and H_{cla} = 0.036 nm^{-1} [51,52] are the bending rigidity and intrinsic curvature of the clathrin coat. The first and second terms on the right-hand side of eqn (3) account for the regions without and with clathrin respectively.

The cytoplasmic domain of the receptor has specific signal sequences that are able to bind with APs promoting the accumulation of clathrin units.[53] With the presence of receptors, the binding affinity between APs and the membrane has been shown to be greatly increased in experiments.[54] The ligand–receptor interactions help stabilize the receptor molecules and may further assist the recruitment of APs. These act as the bridge between the receptors and clathrin lattices on the membrane, and facilitate clathrin accumulation.[55,56] In addition, studies have also observed continuous growth of CCPs during CME, indicating the continuous accumulation of clathrin units and a steady increase of the CCP area during the internalization.[57] Based on those facts, we model the accumulation of clathrin lattices as a ligand–receptor dependent process. Each time a new ligand–receptor bond is formed, a clathrin lattice appears at the new binding site and the effect is represented as a clathrin induced intrinsic curvature field. The affected field will cover a circular area with a radius of 14 nm on the membrane surface according to experiments.[58] Moreover, the local clathrin coats will be dissembled when the nanoparticle is completely detached from the membrane.

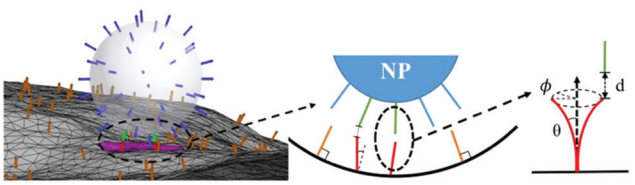

Fig. 2 Schematic of the binding of the ligand (blue) coating nanoparticle (NP) to the cell membrane. The membrane is discretised by a triangulated system containing vertices and links. The binding is mediated by the interactions between the bonded ligands (green) and receptors (red) when the corresponding tip distances d are within the reaction cut-off range. The bonded receptors are allowed to bend and rotate in θ and ϕ. The ligand–receptor binding introduces the clathrin-coated pit (pink) on the membrane. The unbonded receptors (orange) can freely diffuse on the membrane.

We assume monovalent and stochastic binding between the ligand and receptor. The ligand–receptor interactions are modeled by the Bell model:[59]

$$\Delta G_{\mathrm{r}}(d) = \Delta G_0 + \frac{1}{2}kd^2 \qquad (4)$$

Here d is the distance between the binding tips of the interacting ligand and receptor (see Fig. 2), ΔG_0 is the equilibrium free energy change at $d = 0$, and k is the interaction bond force constant. ΔG_0 is obtained from the dissociation constant K_{d} *via* $\Delta G_0 = -k_{\mathrm{B}}T \ln K_{\mathrm{d}}$, where k_{B} is the Boltzmann constant and T is the thermodynamic temperature. We also account for the flexural movement of the receptors during ligand–receptor binding since it is directly related to the entropy change. For a bonded receptor, it is allowed to bend and rotate (Fig. 2). Under the assumption of small deformations, we model the flexure of a receptor as bending a beam from the equilibrium (normal to the membrane surface) position, and the bending energy is calculated as:

$$\Delta G_{\mathrm{f}}(\theta) = (2\mathrm{EI}/L)\theta^2 \qquad (5)$$

where EI is the receptor flexural rigidity, L is the receptor length and θ represents the bending angle from the normal direction of the local membrane. When the binding tips between a ligand–receptor pair are close, bond formation is possible. An arbitrary flexural bending angle θ is selected, and then the distance between the tips (d) is measured. When d is less than the reaction cut-off range (Table 3), the total energy change, including the reaction energy from eqn (4) and receptor bending energy from eqn (5), is calculated and then is used to determine whether the bond formation is accepted or rejected. The existing ligand–receptor bonds may also break according to the energy change (eqn (4) and (5)) during breakage. Once the bond breaks, the receptor returns to the normal direction. More details regarding the clathrin-mediated endocytosis model can be found in our previous publication.[32]

The simulations contain four types of Monte Carlo (MC) steps: receptor diffusion, particle translation or rotation, bond formation or breakage, and membrane surface evolution. In each MC step, a movement will be randomly selected and the system energy (U) is calculated for the new configuration. U_{new} includes the membrane elastic energy E, ligand–receptor interaction energy G_{r}, and receptor flexural energy G_{f}. The new configuration is accepted with the following probability: $\min\{1, \exp[-(U_{\mathrm{new}} - U_{\mathrm{old}})/k_{\mathrm{B}}T]\}$.

3 Results and discussion

In our simulations we adopt the transferrin (Tf)–transferrin receptor (TfR) parameters for ligand–receptor interactions,

since they are well known for triggering CME and have been extensively studied for drug delivery across the blood–brain barrier (BBB).[60–64] We focus on ellipsoidal nanoparticles because they have been used for drug delivery purposes.[4] However, this model can be easily extended to study other nonspherical nanoparticles. The ellipsoidal nanoparticles in our study have the same volume as 80 nm-diameter spherical particles. Based on our previous studies,[32] 80 nm-diameter ligand-coated spherical particles are highly likely to be internalized during CME. The ligand density for all various shape particles is set to be 5300 μm^{-2}.[65] The initial attack angles are set at $\alpha_z = 0$, which means the vector $\boldsymbol{n}$ is parallel to the z-axis at the beginning of the simulations (Fig. 1). For each case, we run at least 5 independent simulations for statistical consistency. Some of the other parameters used in the simulation are shown in Appendix A.

3.1 Endocytosis of oblate-shaped ellipsoids

We first consider the CME of oblate-shaped nanoparticles with $1 < AR < 3$. Table 1 shows the aspect ratio and size parameters used for the simulations. The number of ligands coated on the particle surface is calculated based on the surface area of the particle and the ligand density. The a and b are the length of the major and minor axes in eqn (1).

The CME of oblate ellipsoids shows two entry modes: a tip-first mode with minimal rotation (<15 degrees) and a tilted entry mode with moderate rotation (15–45 degrees) as shown in Fig. 3a. But no laying-down (>45 degrees) pattern has been observed in this study. Both the sphere and high AR oblate ellipsoids (AR = 2.08 and AR = 2.62) rotate less than 10 degrees throughout the simulations. The sphere has less rotation due to the homogeneously distributed curvatures. For high AR oblate ellipsoids, the flat tip with low curvature helps stabilize the nanoparticle on the membrane with less rotation. Small to intermediate AR oblate ellipsoids (AR = 1.17 and AR = 1.47) are capable of taking advantage of both tip-first and tilted entry modes.

As shown in Fig. 3b, the number of ligand–receptor bonds for spherical nanoparticles continuously increases without significant interruptions. The nanoparticle is fully endocytosed after 1.2×10^9 MC steps. For the tip-first and tilted entries of particles with AR = 1.17 and AR = 1.47, the number of bonds shows a two-step growth pattern with two major bond forming periods separated by a plateau in between. The oblate ellipsoid with AR = 1.17 has an initial rapid bond forming period because of the large contact area of the flat tip surface. But the number of bonds reaches a plateau when half of the coated ligands are bonded. This period ends with further growth of the CCP and membrane deformation. The nanoparticle is quickly wrapped with the number of bonds jumping from 40 to 80. The ellipsoid with AR = 1.47 follows a similar two-step bond formation pattern. The main difference is that the first plateau lasts for many more MC steps due to sharper edges. For the tip-first entry of high AR ellipsoids (AR = 2.08 and AR = 2.62), the number of bonds is saturated at around 40 after initial bond formation on the flat tip surface near the membrane.

Table 1 Shape and size parameters for oblate ellipsoids

Aspect ratio (AR)	a (nm)	b (nm)	Number of ligands
1	40	40	106
1.17	42	36	106
1.47	45.5	31	110
2.08	51	24.5	118
2.62	55	21	126

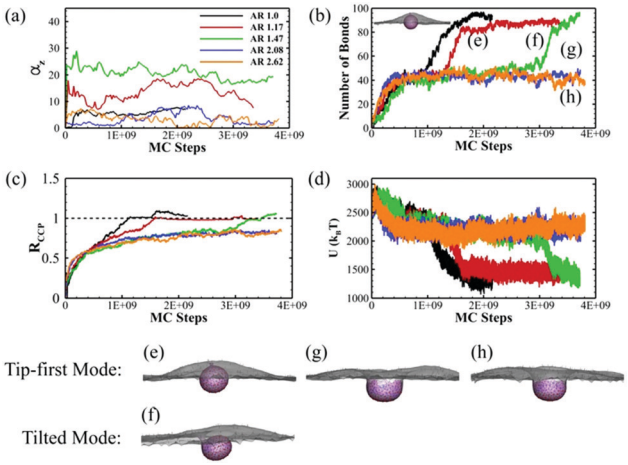

Fig. 3 Endocytosis of sphere and oblate ellipsoids with various aspect ratios. (a) The rotation of the nanoparticle (α_z); (b) the number of ligand–receptor bonds (the equilibrium profile of a spherical nanoparticle is also shown); (c) the normalized CCP area ratio R_{CCP}; and (d) the total energy of the system U as a function of MC steps during CME. The equilibrium particle–membrane profiles for ellipsoids with (e) AR = 1.17, (f) AR = 1.47, (g) AR = 2.08 and (h) AR = 2.62. The CCP (pink region), bonded TfR (red dots), free TfR (black dots), bonded Tf (green dots) and unbonded Tf (blue dots) are all shown in the profiles.

The normalized CCP ratio, R_{CCP}, reflects a similar trend to the number of bonds formed (Fig. 3c). R_{CCP} is defined as the area of the CCP over the area of the minimal ellipsoid that encapsulates the particle. For AR = 1.17 and AR = 1.47 oblate particles, the CCP growth rate significantly drops after $R_{CCP} \sim 0.5$. The flat tip of oblate ellipsoids makes it easy to wrap half of the particle. The growth rate is reduced because of the highly curved edges. After overcoming the curved edge, the CCP growth is accelerated until full wrapping with $R_{CCP} \sim 1.0$. For high aspect ratio ellipsoids, the CCP area also grows fast at the beginning until $R_{CCP} \sim 0.5$. It slowly reaches the maximum value of $R_{CCP} \sim 0.8$ during the rest of the simulation. As shown in Fig. 3d, the decrease of the total energy is mainly driven by the increase of existing bonds in the simulation. Therefore, the energy change follows a subsequent two-step decrease pattern for low to intermediate AR particles. In contrast, the system energy of high AR particles reaches equilibrium rapidly after an initial decrease.

Fig. 3e, g and h show the equilibrium profiles of particles with a tip-first entry mode. The AR = 1.17 particle shows a fully wrapped profile (Fig. 3e) with a symmetric vesicle at equilibrium. For high aspect ratio ellipsoids with AR = 2.08 and AR = 2.62, we observe firm attachment of the particle to the membrane but no internalization (Fig. 3g and h). The membrane partially wraps the oblate with $R_{CCP} < 1.0$ and

further bending is suppressed by the highly curved edges. The ellipsoid shows minimal rotation ($\alpha_z < 10$ degrees) and symmetric wrapping. This is due to an initial large contact area with respect to the membrane surface, which leads to higher adhesion stability and less rotation. The results are consistent with the theoretical work from Bahrami,[66] in which higher adhesion strength is required for high aspect ratio ellipsoids to be internalized. Another theoretical study also proposed a similar prediction that an increased aspect ratio makes it easier for attachment but more difficult to achieve a completely wrapped state for the ellipsoidal nanoparticle.[30] The vesicle formed by the oblate ellipsoid with AR = 1.47 through a tilted entry mode is shown in Fig. 3f. In this situation, the nanoparticle adjusts itself to a tilted position around 20–25 degrees to help bond formation on one side of the edge. Similar rotation of oblate-shaped ellipsoids during RME has also been observed in ref. 25 and 29. The tilting of the ellipsoid leads to an asymmetric wrapping of the membrane.

The internalization of the oblate ellipsoid with AR = 1.17 can take both tip-first and tilted entry modes. Fig. 4 shows the detailed comparison between these two modes. As shown, compared with tip-first entry, a large degree of rotation (40 to 45 degrees) during the early stage leads to tilted entry. The rotation helps bond formation on one side of the curved edges but makes it more difficult for further bond formation on the flat surface. The bond formation reaches a plateau quickly with only ~10 bonds. The formation of the plateau period is the result of the inhomogeneously distributed curvatures on oblate nanoparticles. After quick bond formation, the nanoparticle stays partially wrapped before the membrane could overcome the highly curved edges (Fig. 4d(1)). Driven by the spontaneous deformation of the CCP, the membrane is further bent gradually near the edge (Fig. 4d(2)). After overcoming the bending energy barrier introduced by the curved edges, the free receptors can bind with the ligands on the other side of the oblate ellipsoid (Fig. 4d(3)). The total energy change of the system indicates the energy reduction from the ligand–receptor bindings during the simulation (Fig. 4c). The system energy decreases dramatically after the plateau period, showing the important role of the thermodynamic driving force in determining internalization. During the internalization, the oblate ellipsoid simultaneously adjusts its orientation with respect to the membrane to accommodate the wrapping. As shown in Fig. 4d and e, the tilted nanoparticle forms an asymmetric mature vesicle due to extensive reorientation while the tip-first mode follows a more symmetric membrane wrapping.

3.2 Endocytosis of prolate-shaped ellipsoids

In this section we investigate the CME of prolate-shaped nanoparticles with aspect ratios of $0.25 < AR < 1$. The geometrical parameters of the particles are shown in Table 2.

As shown in Fig. 5a, we also observe two entry modes for prolate-shaped nanoparticles: tip-first and laying-down modes. The tip-first mode is chosen by high to intermediate aspect

Table 2 Shape and size parameters for prolate ellipsoids

Aspect ratio (AR)	a (nm)	b (nm)	Number of ligands
1	40	40	106
0.9	38.5	43	106
0.67	35	52	108
0.42	30	71	118
0.25	25	102	136

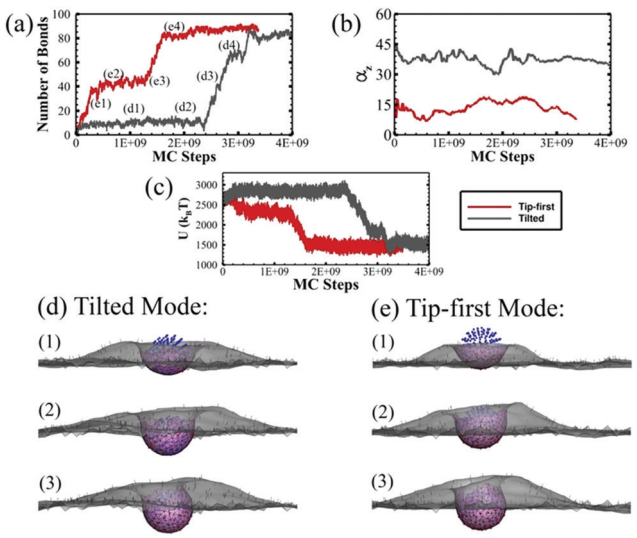

Fig. 4 Two entry modes (tip-first and tilted) of the oblate ellipsoid with AR = 1.17. (a) The number of ligand–receptor bonds; (b) the rotation of the particle (α_z); (c) the total energy of the system U as a function of MC steps during CME. (d and e) The membrane–particle profiles at different stages identified in (a). The CCP (pink region), bonded TfR (red dots), free TfR (black dots), bonded Tf (green dots) and unbonded Tf (blue dots) are all shown in the profiles.

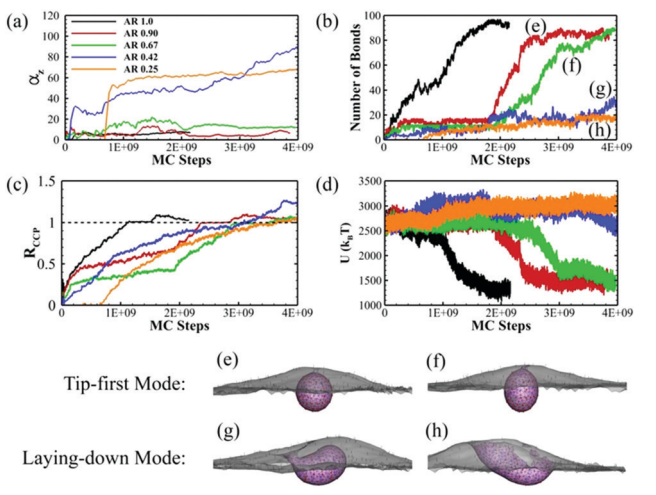

Fig. 5 Endocytosis of sphere and prolate-shaped ellipsoids with different aspect ratios. (a) The rotation of the nanoparticle (α_z); (b) the number of ligand–receptor bonds; (c) the normalized CCP area ratio R_{CCP}; and (d) the total energy of the system U as a function of MC steps during CME. The equilibrium particle–membrane profiles for ellipsoids with (e) AR = 0.90, (f) AR = 0.67, (g) AR = 0.42 and (h) AR = 0.25. The CCP (pink region), bonded TfR (red dots), free TfR (black dots), bonded Tf (green dots) and unbonded Tf (blue dots) are all shown in the profiles.

ratio particles with AR = 0.9 and AR = 0.67, characterized by a two-step growth pattern of bonds (Fig. 5b). Since the tip of the prolate particle is highly curved, the bond formation reaches a plateau quickly at $\sim 2 \times 10^8$ MC steps with less than 20 ligand–receptor bonds. The periods of the plateau are similar for both AR = 0.9 and AR = 0.67 ellipsoids. This is quite different from the oblate-shaped cases where a higher AR particle has a significantly longer plateau period than a smaller AR one (see Fig. 3b). After 2.0×10^9 MC steps, the number of bonds quickly increases to more than 80 for both cases due to the easiness of bond formation on the flat edges of the prolate ellipsoid. The R_{CCP} and system energy U also follow a similar step-wise change in the simulations (Fig. 5c and d). During the wrapping, the ellipsoid remains perpendicular to the membrane surface with little rotation. The vesicle formed by the nanoparticle with AR = 0.9 is mostly spherically shaped, while it becomes an ellipsoidal shape for the ellipsoid with AR = 0.67 due to the lower aspect ratio (Fig. 5e and f).

On the other hand, the low aspect ratio nanoparticles with AR = 0.42 and AR = 0.25 use the laying-down entry mode during which the particles rotate to a nearly horizontal position (Fig. 5a). The number of bonds during the uptake is much lower than the tip-first mode (Fig. 5b). As a result, the total energies of the systems U do not decrease (Fig. 5d). However, R_{CCP} still keeps growing during the simulation (Fig. 5c). The AR = 0.42 ellipsoid is fully wrapped while the AR = 0.25 ellipsoid does not completely internalize (Fig. 5g and h). Though the R_{CCP} of the AR = 0.25 particle also reaches 1.0, the CCP cannot bend itself to fully wrap the particle because of the extremely low aspect ratio.

Our results indicate that prolate ellipsoids with low AR prefer to take the laying-down mode to enter cells. Experiments have observed both tip-first and laying-down entry modes for viruses with low AR.[67,68] Coarse-grained molecular dynamics (CGMD) studies also showed a similar perpendicular to parallel reorientation of low AR spherocylinders in RME.[69] A more recent theoretical study also showed that the parallel orientation of ellipsoids is more energetically favorable than the tip-first orientation because of a higher bending energy cost per area at the tip.[24] However, the theoretical work from Yi *et al.*[70] and CGMD simulations from Shen *et al.*[25] showed that the low AR ellipsoids preferred the tip-first entry mode at low membrane tension. In ref. 70, the ligand–receptor interactions have been modeled as direct adhesion within a certain area and the membrane wrapping was driven by the energy reduction caused by the adhesion. In ref. 25, discrete ligand–receptor interactions have been considered with a relatively high binding strength (50 k_BT) and very long interaction cutoff (37.5 nm). In our model, the ligand–receptor interaction cutoff is much shorter, therefore it is much harder to continuously form bonds from a tip-oriented position with high curvatures. Laying-down helps bond formation on the flat side and further reduces the energy of the system.

Another interesting observation with AR = 0.42 and AR = 0.25 particles is that R_{CCP} continuously increases while the number of ligand–receptor bonds remains nearly constant at a relatively low value (less than 30) (Fig. 5b and c). In our model, the recruitment and accumulation of clathrin are stimulated by the formation of new ligand–receptor bonds (see the methods section). Laying-down of the particle allows continuous new ligand–receptor bond formation at new binding sites. However, the existing bonds break more frequently at the same time. This is due to the fact that the radius of curvature on the membrane caused by the clathrin (H_{cla}) is $\sim$30 nm; this is significantly smaller than the b values of the ellipsoids (71 nm and 102 nm for AR = 0.42 and AR = 0.25 particles). Therefore, the bending of the membrane caused by clathrin tends to break the existing ligand–receptor bonds. As a result, the prolate ellipsoid with AR = 0.42 is fully wrapped with only $\sim$30 bonds, less than half of the spherical counterpart at equilibrium. As shown in Fig. 5d, we do not observe a significant total energy decrease, which is similar to the high AR oblate ellipsoid case in Fig. 3d. The ability to be internalized with fewer ligand–receptor bonds is important to transcellular drug delivery. For transcellular drug delivery, the nanoparticles need to first enter the cell at one side and then release from the cell at the other side. Fewer ligand–receptor bonds during internalization facilitates the particle release during expulsion. Indeed, experiments have demonstrated that spherical nanoparticles with lower avidity have better efficiency for transcytosis across blood–brain barriers.[65,71] In addition, it has also been observed in *in vivo* experiments that it is easier for Tf-coated nanorods to release from the cell than spherical ones.[7]

Moreover, for the ellipsoid with intermediate aspect ratio AR = 0.67, we find that the particle can be internalized by all three modes. Fig. 6 presents the entry of tip-first and laying-down modes. Compared with the two-step growth of bonds in the tip-first mode, the laying-down mode features a continuous increase of bonds until it is fully endocytosed. The internalization of the laying-down ellipsoid takes less MC steps than the tip-first mode. This is because the rotation of the particle allows the ligands on the flat side to interact with the receptors on the membrane. The equilibrium energy of the tip-first mode is lower than the laying-down mode, meaning that the tip-first mode is a more energetically favorable status for this ellipsoidal nanoparticle.

3.3 Overall endocytosis comparison

Fig. 7 summarizes our findings of endocytosis for ellipsoid particles. As shown in Fig. 7a, there are three major patterns for the entry of ellipsoids with different aspect ratios. Characterized by the degrees of rotation during the entry, we observe a tip-first mode ($<$15 degrees), tilted entry mode (15–45 degrees) and laying-down mode ($>$45 degrees). The oblate ellipsoid with AR $>$ 1.47 only takes the tip-first entry mode. On the other hand, the low aspect ratio prolate nanoparticles with AR = 0.25 and AR = 0.42 only use the laying-down entry mode. Intermediate aspect ratio ellipsoids with $0.67 \leq$ AR ≤ 1.47 may choose either the tip-first mode or the tilted entry mode. Interestingly the prolate ellipsoid with AR = 0.67 shows flexibility and may take any of the three entry modes for endocytosis. The capability of taking any entry mode is helpful for drug delivery applications. In realistic biological scenarios, the initial contact direction between the particle and cell membrane is random.

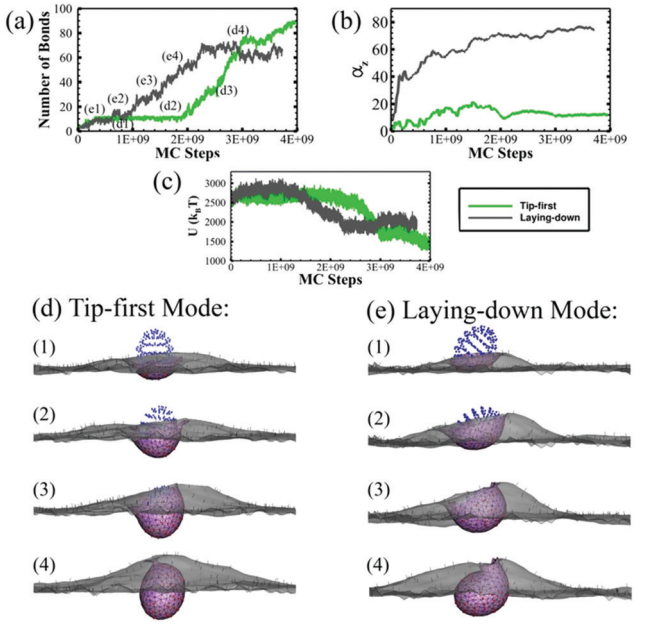

Fig. 6 Two entry modes of the prolate ellipsoid with AR = 0.67. (a) The number of ligand–receptor bonds; (b) the rotation of the particle (α_z); and (c) the total energy of the system U as a function of MC steps during CME. (d and e) The membrane–particle profiles at different stages identified in (a). The CCP (pink region), bonded TfR (red dots), free TfR (black dots), bonded Tf (green dots) and unbonded Tf (blue dots) are all shown in the profiles.

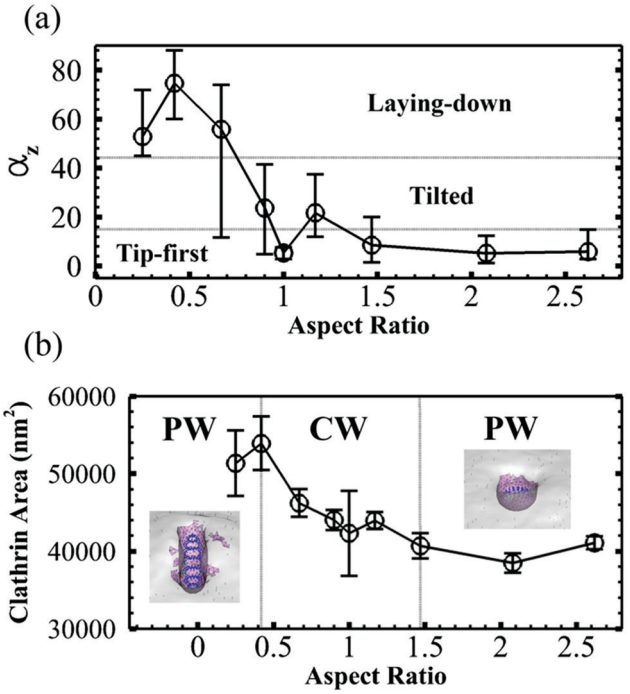

Fig. 7 Equilibrium rotation angles and clathrin coated area for spherical and ellipsoidal nanoparticles. (a) The nanoparticles show three entry patterns: tip-first mode (<15 degrees), tilted entry mode (15–45 degrees) and laying-down mode (>45 degrees) depending on the degree of rotation. The error bars represent the minimal and maximal degrees of rotation observed in 5 independent simulations. (b) The clathrin area plot shows the influence of the shape of nanoparticle on the internalization capability. The error bars are based on the standard deviation from 5 independent simulations. The nanoparticle is able to be completely wrapped (CW) within $0.42 \leq AR \leq 1.47$ while only partially wrapped (PW) for $AR < 0.42$ or $AR > 1.47$. The equilibrium membrane profiles for nanoparticles with AR = 0.25 and 2.62 are shown respectively.

Therefore particles that can adopt all entry modes may have better opportunities to enter the cells. Overall the prolate nanoparticles rotate more to enter the cell compared with the sphere and oblate nanoparticles during endocytosis, because of the highly curved tip of prolate ellipsoids.

Fig. 7b summarizes the internalization stages of all the particles with different shapes. We have observed complete wrapping (CW) for nanoparticles with aspect ratio $0.42 \leq AR \leq 1.47$. The sphere nanoparticle can be internalized with the least MC steps indicating the highest efficiency. Although it is more difficult for ellipsoidal particles to enter the cell, in general they require fewer ligand–receptor bonds compared with spherical particles. Especially, the prolate ellipsoid with AR = 0.42 can have CW with a significantly lower number of bonds ($\sim$30). This is especially important for transcellular drug delivery since fewer bonds during endocytosis may lead to a higher exocytosis efficiency. Overall, our results are consistent with the experimental observations;[6,7] low AR prolate and high AR oblate nanoparticles, with $AR < 0.42$ or $AR > 1.47$ in our study, only show partial wrapping (PW), indicating a low internalization efficiency.

The rotation of the particles, different entry modes and wrapping states during endocytosis on fluid membranes have been studied through various analytical analysis and simulations.[24,25,29,30,66,69,72] The distinctive feature of our model is that the deformation of the membrane and wrapping of the particles are driven by the assembly of CCPs. In our model, the accumulation of CCPs is triggered by the ligand–receptor interactions, while the ligand–receptor binding is modeled as a stochastic process and the modelling parameters are directly obtained from experiments. Therefore, the entire particle internalization process is stochastic and dictated by many inter-correlated events, such as ligand–receptor bond formation/breakage, particle translation/rotation, clathrin assembly/dissembly, membrane deformation, *etc.* As a result, our simulations provide additional information. For example, our results indicate that the internalization of particles may not always correlate with continuous increasing of bonds in CME (see Fig. 3). The rotation (or entry mode) of the same nanoparticle may be different due to localized CCP recruitment. Indeed, our results indicate that multiple entry modes may be taken by specific nanoparticles. Due to the stochastic nature, the wrapping state of certain particles may also become scattered.

4 Conclusions

CME is the fundamental biological mechanism for the cell metabolism and intracellular transport of nanoparticles. The advancement of nanotechnology makes the manufacturing of nanoparticles with different shapes possible for biomedical

application. But how the different shape nanoparticles interact with the cell membrane is complicated and still under debate. In this work, we systematically investigated the CME of transferrin-coated spherical and ellipsoidal nanoparticles through modeling and simulations. Our stochastic model takes into account the membrane deformation, clathrin lattice accumulation and transferrin–transferrin receptor interactions based on Monte Carlo simulations. In our model, the membrane deformation and particle internalization are primarily driven by the clathrin polymerization, which is stimulated from the ligand–receptor interactions.

Through our simulations, we found three entry modes for the CME of spheres and ellipsoids including tip-first, tilted entry and laying-down modes. Each mode is characterized by distinctive degrees of rotation during the wrapping of the membrane. High aspect ratio oblate ellipsoids with AR $>$ 2 use only the tip-first entry mode. Small to intermediate aspect ratio ellipsoids with $0.67 \leq \mathrm{AR} \leq 1.47$ are able to take the tip-first and tilted entry modes. Low aspect ratio prolate nanoparticles with AR $<$ 0.5 only internalize through the laying-down mode. Moreover, we have observed that certain moderate aspect ratio prolate ellipsoids, such as AR = 0.67 in our study, are able to take advantage of all three modes for internalization.

The bond formation and CCP growth of both tip-first and tilted modes show a two-step wrapping pattern with a plateau in between. The plateau period depends on the aspect ratio and rotation of the nanoparticle. The laying-down mode has a continuous CCP wrapping pattern, but the equilibrium number of bonds is highly dependent on the aspect ratio of the nanoparticle. The prolate ellipsoid with AR = 0.42 is internalized with more MC steps but much fewer ligand–receptor bonds than other shapes. Internalization of nanoparticles with fewer ligand–receptor bonds may significantly facilitate release of the particle during transcellular drug delivery. In addition, we have observed complete wrapping for particles with an intermediate AR range of $0.42 \leq \mathrm{AR} \leq 1.47$. In general, the internalization of spherical nanoparticles is easier than that of ellipsoidal particles. In summary, our simulation results are consistent with a variety of experimental measurements and provide deeper understanding of the fundamental mechanisms involved in CME of nanoparticles with different shapes. Our model represents a powerful and viable platform for facilitating the rational design of nanoparticles for targeted drug delivery.

Conflicts of interest

There are no conflicts to declare.

Appendix A: Simulation parameters

The table below lists some of the simulation parameters used and the corresponding references:

Table 3 Summary of some parameters used in the simulation

Parameters	Value	Ref.
Size of membrane surface	910 nm × 910 nm	
Membrane bending rigidity κ	20 k_BT	73
Membrane characteristic tension σ	0.001 pN nm^{-1}	74
Clathrin bending rigidity κ_{cla}	200 k_BT	75
Clathrin intrinsic curvature H_{cla}	0.036 nm^{-1}	51
Transferrin receptor length	9.3 nm	76
Transferrin receptor radius	5 nm	76
Antibody length	9 nm	77
Antibody radius	2.5 nm	77
Number of transferrin receptors on the luminal side	300	78
Equilibrium free energy change ΔG_0	-8.64×10^{-20} J	79
Reactive compliance (reaction cut-off distance)	0.9 nm	79
Receptor flexural rigidity EI	7000 pN nm^2	80
System temperature	298 K	

Acknowledgements

The research reported in this publication was supported by the National Science Foundation under CBET-1604211 and the National Institute of General Medical Sciences of the National Institutes of Health under Award Number R01GM122081. Computational resources were provided in part by the Extreme Science and Engineering Discovery Environment (XSEDE) under grant No. MCB170012.

References

1 B. D. Harrison, T. M. A. Wilson and A. Klug, *Philos. Trans. R. Soc. London, Ser. B*, 1999, **354**, 531–535.
2 G. Wanger, T. C. Onstott and G. Southam, *Geobiology*, 2008, **6**, 325–330.
3 N. Doshi and S. Mitragotri, *PLoS One*, 2010, **5**, e10051.
4 Y. Liu, J. Tan, A. Thomas, D. Ou-Yang and V. R. Muzykantov, *Ther. Delivery*, 2012, **3**, 181–194.
5 L. Xu, H. Kuang, L. Wang and C. Xu, *J. Mater. Chem.*, 2011, **21**, 16759–16782.
6 B. D. Chithrani, A. A. Ghazani and W. C. W. Chan, *Nano Lett.*, 2006, **6**, 662–668.
7 B. D. Chithrani and W. C. W. Chan, *Nano Lett.*, 2007, **7**, 1542–1550.
8 L. Florez, C. Herrmann, J. M. Cramer, C. P. Hauser, K. Koynov, K. Landfester, D. Crespy and V. Mailänder, *Small*, 2012, **8**, 2222–2230.
9 Y. Zhang, S. Tekobo, Y. Tu, Q. Zhou, X. Jin, S. A. Dergunov, E. Pinkhassik and B. Yan, *ACS Appl. Mater. Interfaces*, 2012, **4**, 4099–4105.
10 S. Barua, J.-W. Yoo, P. Kolhar, A. Wakankar, Y. R. Gokarn and S. Mitragotri, *Proc. Natl. Acad. Sci. U. S. A.*, 2013, **110**, 3270–3275.
11 X. Huang, X. Teng, D. Chen, F. Tang and J. He, *Biomaterials*, 2010, **31**, 438–448.
12 H. Meng, S. Yang, Z. Li, T. Xia, J. Chen, Z. Ji, H. Zhang, X. Wang, S. Lin, C. Huang, Z. H. Zhou, J. I. Zink and A. E. Nel, *ACS Nano*, 2011, **5**, 4434–4447.

13 S. E. A. Gratton, P. A. Ropp, P. D. Pohlhaus, J. C. Luft, V. J. Madden, M. E. Napier and J. M. DeSimone, *Proc. Natl. Acad. Sci. U. S. A.*, 2008, **105**, 11613–11618.
14 R. Agarwal, V. Singh, P. Jurney, L. Shi, S. V. Sreenivasan and K. Roy, *Proc. Natl. Acad. Sci. U. S. A.*, 2013, **110**, 17247–17252.
15 R. Agarwal, P. Jurney, M. Raythatha, V. Singh, S. V. Sreenivasan, L. Shi and K. Roy, *Adv. Healthcare Mater.*, 2015, **4**, 2269–2280.
16 S. Dasgupta, T. Auth and G. Gompper, *J. Phys.: Condens. Matter*, 2017, **29**, 373003.
17 S. Zhang, H. Gao and G. Bao, *ACS Nano*, 2015, **9**, 8655–8671.
18 C. Kinnear, T. L. Moore, L. Rodriguez-Lorenzo, B. Rothen-Rutishauser and A. Petri-Fink, *Chem. Rev.*, 2017, **117**, 11476–11521.
19 J. Zhao and M. H. Stenzel, *Polym. Chem.*, 2018, **9**, 259–272.
20 R. Qiao, A. P. Roberts, A. S. Mount, S. J. Klaine and P. C. Ke, *Nano Lett.*, 2007, **7**, 614–619.
21 K. Yang and Y.-Q. Ma, *Nat. Nanotechnol.*, 2010, **5**, 579.
22 S. Nangia and R. Sureshkumar, *Langmuir*, 2012, **28**, 17666–17671.
23 R. Vácha, F. J. Martinez-Veracoechea and D. Frenkel, *Nano Lett.*, 2011, **11**, 5391–5395.
24 S. Dasgupta, T. Auth and G. Gompper, *Nano Lett.*, 2014, **14**, 687–693.
25 Z. Shen, H. Ye, X. Yi and Y. Li, *ACS Nano*, 2019, **13**, 215–228.
26 Y. Li, T. Yue, K. Yang and X. Zhang, *Biomaterials*, 2012, **33**, 4965–4973.
27 C. Huang, Y. Zhang, H. Yuan, H. Gao and S. Zhang, *Nano Lett.*, 2013, **13**, 4546–4550.
28 L. Zhang, Y. Zhao and X. Wang, *ACS Appl. Mater. Interfaces*, 2017, **9**, 26665–26673.
29 H. Tang, H. Zhang, H. Ye and Y. Zheng, *J. Phys. Chem. B*, 2018, **122**, 171–180.
30 S. Dasgupta, T. Auth and G. Gompper, *Soft Matter*, 2013, **9**, 5473–5482.
31 L. Chen, S. Xiao, H. Zhu, L. Wang and H. Liang, *Soft Matter*, 2016, **12**, 2632–2641.
32 H. Deng, P. Dutta and J. Liu, *Biochim. Biophys. Acta, Gen. Subj.*, 2018, **1862**, 2104–2111.
33 W. Helfrich, *Z. Naturforsch., C: Biochem., Biophys., Biol., Virol.*, 1973, **28**, 693–703.
34 M. Deserno, *Phys. Rev. E: Stat., Nonlinear, Soft Matter Phys.*, 2004, **69**, 031903.
35 J. Agudo-Canalejo and R. Lipowsky, *ACS Nano*, 2015, **9**, 3704–3720.
36 Q. Yu, S. Othman, S. Dasgupta, T. Auth and G. Gompper, *Nanoscale*, 2018, **10**, 6445–6458.
37 J. Liu, R. Tourdot, V. Ramanan, N. J. Agrawal and R. Radhakrishanan, *Mol. Phys.*, 2012, **110**, 1127–1137.
38 O. L. Mooren, B. J. Galletta and J. A. Cooper, *Annu. Rev. Biochem.*, 2012, **81**, 661–686.
39 B. Qualmann, M. M. Kessels and R. B. Kelly, *J. Cell Biol.*, 2000, **150**, F111–F116.
40 G. Gompper and D. M. Kroll, *J. Phys.: Condens. Matter*, 1997, **9**, 8795–8834.
41 D. M. Kroll and G. Gompper, *Science*, 1992, **255**, 968.
42 N. Ramakrishnan, P. B. S. Kumar and J. H. Ipsen, *Phys. Rev. E: Stat., Nonlinear, Soft Matter Phys.*, 2010, **81**, 041922.
43 J. H. Hurley, E. Boura, L. A. Carlson and B. Rozycki, *Cell*, 2010, **143**, 875–887.
44 A. Fotin, Y. F. Cheng, P. Sliz, N. Grigorieff, S. C. Harrison, T. Kirchhausen and T. Walz, *Nature*, 2004, **432**, 573–579.
45 L. Hinrichsen, A. Meyerhoiz, S. Groos and E. J. Ungewickell, *Proc. Natl. Acad. Sci. U. S. A.*, 2006, **103**, 8715–8720.
46 R. J. Mashl and R. F. Bruinsma, *Biophys. J.*, 1998, **74**, 2862–2875.
47 T. Kohyama, D. M. Kroll and G. Gompper, *Phys. Rev. E: Stat., Nonlinear, Soft Matter Phys.*, 2003, **68**, 061905.
48 M. F. Hagan and D. Chandler, *Biophys. J.*, 2006, **91**, 42–54.
49 M. Giani, W. K. den Otter and W. J. Briels, *Biophys. J.*, 2016, **111**, 222–235.
50 A. Banerjee, A. Berezhkovskii and R. Nossal, *Biophys. J.*, 2012, **102**, 2725–2730.
51 S. Zaremba and J. H. Keen, *J. Cell Biol.*, 1983, **97**, 1339–1347.
52 M. G. J. Ford, I. G. Mills, B. J. Peter, Y. Vallis, G. J. K. Praefcke, P. R. Evans and H. T. McMahon, *Nature*, 2002, **419**, 361–366.
53 J. S. Bonifacino and L. M. Traub, *Annu. Rev. Biochem.*, 2003, **72**, 395–447.
54 D. Ricotta, S. D. Conner, S. L. Schmid, K. von Figura and S. Höning, *J. Cell Biol.*, 2002, **156**, 791–795.
55 J. Schlessinger, *Cell*, 2000, **103**, 211–225.
56 J. Chen, J. Wang, K. R. Meyers and C. A. Enns, *Traffic*, 2009, **10**, 1488–1501.
57 M. Ehrlich, W. Boll, A. van Oijen, R. Hariharan, K. Chandran, M. L. Nibert and T. Kirchhausen, *Cell*, 2004, **118**, 591–605.
58 J. Heuser and T. Kirchhausen, *J. Ultrastruct. Res.*, 1985, **92**, 1–27.
59 G. I. Bell, M. Dembo and P. Bongrand, *Biophys. J.*, 1984, **45**, 1051–1064.
60 A. Dautry-Varsat, A. Ciechanover and H. F. Lodish, *Proc. Natl. Acad. Sci. U. S. A.*, 1983, **80**, 2258–2262.
61 Z. M. Qian, H. Y. Li, H. Z. Sun and K. Ho, *Pharmacol. Rev.*, 2002, **54**, 561–587.
62 H. Y. Li, H. Z. Sun and Z. M. Qian, *Trends Pharmacol. Sci.*, 2002, **23**, 206–209.
63 D. Peer, J. M. Karp, S. Hong, O. C. FaroKhzad, R. Margalit and R. Langer, *Nat. Nanotechnol.*, 2007, **2**, 751–760.
64 A. I. Khan, J. Liu and P. Dutta, *Biochim. Biophys. Acta, Gen. Subj.*, 2018, **1862**, 1168–1179.
65 D. T. Wiley, P. Webster, A. Gale and M. E. Davis, *Proc. Natl. Acad. Sci. U. S. A.*, 2013, **110**, 8662–8667.
66 A. H. Bahrami, *Soft Matter*, 2013, **9**, 8642–8646.
67 T. Noda, H. Ebihara, Y. Muramoto, K. Fujii, A. Takada, H. Sagara, J. H. Kim, H. Kida, H. Feldmann and Y. Kawaoka, *PLoS Pathog.*, 2006, **2**, e99.
68 S. Welsch, L. Kolesnikova, V. Krähling, J. D. Riches, S. Becker and J. A. G. Briggs, *PLoS Pathog.*, 2010, **6**, e1000875.
69 R. Vacha, F. J. Martinez-Veracoechea and D. Frenkel, *Nano Lett.*, 2011, **11**, 5391–5395.
70 X. Yi, X. Shi and H. Gao, *Nano Lett.*, 2014, **14**, 1049–1055.

71 Y. J. Yu, Y. Zhang, M. Kenrick, K. Hoyte, W. Luk, Y. M. Lu, J. Atwal, J. M. Elliott, S. Prabhu, R. J. Watts and M. S. Dennis, *Sci. Transl. Med.*, 2011, **3**, 84ra44.
72 D. M. Richards and R. G. Endres, *Proc. Natl. Acad. Sci. U. S. A.*, 2016, **113**, 6113–6118.
73 E. Evans and W. Rawicz, *Phys. Rev. Lett.*, 1990, **64**, 2094–2097.
74 J. E. Hassinger, G. Oster, D. G. Drubin and P. Rangamani, *Proc. Natl. Acad. Sci. U. S. A.*, 2017, **114**, E1118–E1127.
75 A. J. Jin, K. Prasad, P. D. Smith, E. M. Lafer and R. Nossal, *Biophys. J.*, 2006, **90**, 3333–3344.
76 H. Fuchs, U. Lücken, R. Tauber, A. Engel and R. Geßner, *Structure*, 1998, **6**, 1235–1243.
77 H. M. Berman, J. Westbrook, Z. Feng, G. Gilliland, T. N. Bhat, H. Weissig, I. N. Shindyalov and P. E. Bourne, *Nucleic Acids Res.*, 2000, **28**, 235–242.
78 J. D. Bleil and M. S. Bretscher, *EMBO J.*, 1982, **1**, 351–355.
79 A. Yersin, T. Osada and A. Ikai, *Biophys. J.*, 2008, **94**, 230–240.
80 S. Weinbaum, X. B. Zhang, Y. F. Han, H. Vink and S. C. Cowin, *Proc. Natl. Acad. Sci. U. S. A.*, 2003, **100**, 7988–7995.